# Synthesis, Characterization, and Electrochemical Properties of Magnesium Birnessite and Zinc Chalcophanite Prepared by a Low-Temperature Route

Blake J. Aronson,[†] Andrew K. Kinser,[‡] Stefano Passerini,*[,‡] William H. Smyrl,[‡] and Andreas Stein*[,†]

*Department of Chemistry, University of Minnesota, Minneapolis, Minnesota 55455, and Department of Chemical Engineering and Materials Science, University of Minnesota, Minneapolis, Minnesota 55455*

*Received August 21, 1998. Revised Manuscript Received December 29, 1998*

Magnesium-substituted birnessite and zinc chalcophanite have been synthesized through a novel procedure based on a combination of coprecipitation and metal ion intercalation techniques. The materials showed very promising performance as hosts for lithium intercalation. Upon galvanostatic discharge, Mg−birnessite and Zn−chalcophanite composite cathodes were able to intercalate >2 equiv of lithium per mole.

## Introduction

The birnessites is a class of layered manganese oxides which are both found in nature and produced synthetically. They have been widely studied for their ion-exchange and potential secondary battery applications.[1−5] Birnessite is characterized by a layered structure comprised of edge-sharing $MnO_6$ octahedra, with water molecules and metal cations occupying the interlayer region.[1−3] It is structurally similar to chalcophanite, $ZnMn_3O_4{\cdot}3H_2O$,[6,7] and has an interlayer distance of 7.1 Å. Other forms of Na−birnessite include a dehydrated form with an interlayer spacing of 5.5 Å, and an extrahydrated phase, called buserite, with a spacing of 10 Å, expanded by the presence of an extra layer of water (see Figure 1).[1,6,8] Although the exact formula varies depending on the reaction conditions employed, the stoichiometry for A−birnessite (where A = $H^+$ or metal cation) is described as $A_xMnO_{2-y}{\cdot}zH_2O$ (typically, $x = 0.2-0.7$, $y = -0.16-0.16$, and $z = 0.4-0.8$), and the average oxidization state of the manganese usually falls in the range from 3.6 to 3.8.[1,3,5,9]

The hydrated layer structure of the birnessites allows for facile mobility of the interlayer cations with fast kinetics and little structural rearrangement.[2] Consequently, these materials are of interest for intercalation, ion-exchange, and, most frequently, secondary battery applications. While the layered $LiCoO_2$ is already employed in lithium batteries, Li−birnessite is under intense investigation as a cheaper alternative.[6] It has been shown that lamellar manganese oxides can intercalate as much as 0.8 equivs of lithium at a working potential of around 2.9 V vs Li/$Li^+$ with capacities of up to 200 (mA h)/g.[2,9,11] However, such high capacity materials often degrade rapidly. It has also been observed that sodium-intercalated birnessites give the best electrochemical performance, while poorly crystalline

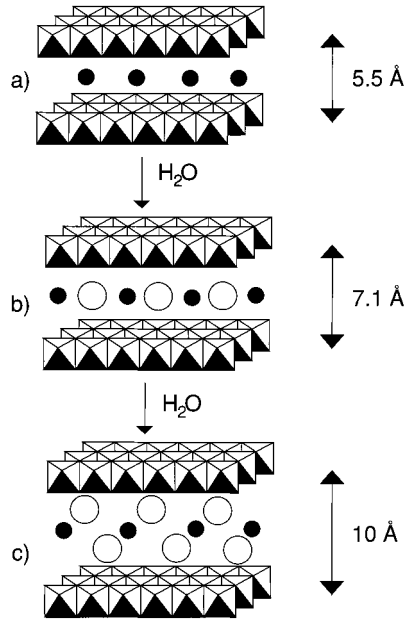


**Figure 1.** Three different phases of layered manganese oxides: (a) the dehydrated phase, (b) the birnessite phase, and (c) the buserite phase. The birnessite phase can be obtained by intercalation of the dehydrated phase with $Mg(NO_3)_2$. Black circles indicate metal cations; white circles, water molecules.

[†] Department of Chemistry.
[‡] Department of Chemical Engineering and Materials Science.

(1) Ching, S.; Petrovay, D. J.; Jorgensen, M. L.; Suib, S. L. *Inorg. Chem.* **1997**, *36*, 883−890.
(2) LeGoff, P.; Baffier, N.; Bach, S.; Pereira-Ramos, J. P. *J. Mater. Chem.* **1994**, *4*, 875−881.
(3) Post, J. E.; Veblen, D. R. *Am. Miner.* **1990**, *75*, 477−489.
(4) Feng, Q. *Chem. Mater.* **1995**, *7*, 1722−1727.
(5) LeGoff, P.; Baffier, N.; Bach, S.; Pereira-Ramos, J. P. *Mater. Res. Bull.* **1996**, *31*, 63−75.
(6) Chen, R.; Zavalij, P.; Whittingham, M. S. *Chem. Mater.* **1996**, *8*, 1275−1280.
(7) Wadsley, A. D. *Acta Crystallogr.* **1955**, *8*, 165−173.
(8) Potter, R. M.; Rossman, G. R. *Am. Miner.* **1979**, *64*, 1199−1218.
(9) Strobel, P. *MRS Symp. Proc.* **1993**, *293*, 63−68.
(10) Bach, S.; Pereira-Ramos, J. P.; Baffier, N. *J. Solid State Chem.* **1995**, *120*, 70−73.
(11) Bach, S.; Pereira-Ramos, J.-P.; Cachet, C.; Bode, M.; Yu, L. T. *Electrochim. Acta* **1995**, *40*, 785−789.

10.1021/cm9805828 CCC: $18.00 
Published on Web 03/13/1999

birnessites and birnessites containing larger cations give the poorest performance.[9] Much study remains on the improvement of birnessites for battery applications.

As mentioned above, Li−birnessite is of greatest interest for lithium cells. However, there is only one reference in the literature of a direct synthesis for Li−birnessite.[12] The Li form is far more commonly obtained by ion exchange with Na−birnessite. Consequently, Na− and K−birnessites have been investigated in greater detail than other layered manganese oxides.[3−6,9,13−15] Studies have also been conducted on the products of ion exchange with other cations.[5,10,16,17]

Na− and K−birnessites have been prepared using several methods. The two most common approaches are the reduction of $NaMnO_4$ or $KMnO_4$, usually by a reducing sugar and under acidic conditions,[1,2,13,14,18] and the oxidation of a Mn(II) salt by air, oxygen, permanganate, or $H_2O_2$ in concentrated NaOH solution.[3,5,9,13,16] The only reported direct syntheses of Li−birnessite involves the latter approach, with NaOH replaced by LiOH.[12] A hydrothermal synthesis, wherein $\alpha$-$Mn_2O_3$ synthesized from $MnCO_3$ was heated in aqueous NaOH solution at 155 °C for several weeks,[19] has been reported, as have electrolytic preparations using manganese(II) acetate and potassium acetate or $MnSO_4$ and $H_2SO_4$ solutions to generate birnessite layers on the electrode surface.[15,20] Other syntheses, such as the acid treatment of $\alpha$-$Na_{0.7}MnO_2$ and $\alpha$-$NaMnO_2$, have also been described.[10] Herein we report a new procedure for the synthesis of Zn− and Mg−birnessites, as well as analysis of these materials by ion exchange, powder XRD, thermogravimetric analysis (TGA), mid-IR and far-IR spectroscopies, and electrochemical studies.

## Experimental Section

**Materials.** Reagents and other materials were obtained from the following sources: manganese(II) acetate tetrahydrate, cyclohexane, and high purity lithium hexafluoroarsenate, Aldrich; zinc nitrate hexahydrate, lithium nitrate, ammonium nitrate, Fisher; sodium nitrate, magnesium nitrate hexahydrate, copper(II) nitrate, cadmium nitrate, Mallinckrodt; nickel nitrate, cobalt(II) nitrate, Baker; silver nitrate and Chempure lithium foil, Foote Mineral Co.; ethylene carbonate (EC) and propylene carbonate (PC), Grant Chemicals (battery grade); Ketjen black carbon (KJB), Akzo Nobel; and polytetrafluorethylene (PTFE), Dupont. All chemicals were used without further purification. All water was distilled and doubly deionized.

**Synthesis of Layered Manganese Oxides.** Zn- and Mg-exchanged manganese oxides were prepared by a combination of coprecipitation and metal ion intercalation techniques. Approximately 44 g manganese(II) acetate tetrahydrate and 15 g sodium nitrate (Mn:Na = 1:1) were dissolved in 200 mL of doubly deionized distilled water. The solution was heated at about 100 °C overnight to evaporate the water. The remaining solid was ground and heated under air at 400 °C for 10 h to produce a dark brown powder. The powder was then stirred at room temperature in an aqueous solution of either 2 M $Zn(NO_3)_2$ or 0.05 M $Mg(NO_3)_2$ overnight, filtered over vacuum, rinsed three times with water, and air-dried at room temperature. The ion-exchange capacities of the products were studied by stirring the solids in 2 M lithium or sodium nitrate solutions overnight at room temperature, followed by vacuum filtration, triple rinsing with water, and air-drying at room temperature.

**Electrochemical Studies.** Prior to electrochemical characterization, the Mg- and Zn-intercalated manganese oxides were dried under vacuum for 2 days at room temperature. Composite cathodes were prepared by mixing Mg−birnessite or Zn−chalcophanite with Ketjen black carbon and poly(tetrafluoroethylene) to obtain the following ratio, birnessite or chalcophanite:KJB:PTFE = 80:10:10. Cyclohexane was added to the mixture of powders to form a slurry which was stirred until a homogeneous suspension was obtained (10−15 h). The slurry was dried by evaporation of the solvent in dry air (relative humidity (RH) < 1%) and then under vacuum ($10^{-3}$ Torr) at room temperature. The dried composite powder was ground in a mortar to form sheets and then roll milled to form a foil. Disks of composite material were punched and compressed at 2 metric tons to form pellets. A typical pellet weighed about 8−12 mg, was 0.10−0.15 mm thick, and 6.5 mm in diameter. The gravimetric density of the pellets was about 2.2 g/cm$^3$ for Mg−birnessite composite cathodes and 2.65 g/cm$^3$ for Zn−chalcophanite composite cathodes. The pellets were pressed onto a folded stainless steel X-met (a net composed of a single sheet of metal) that was used as a current collector.

The composite cathodes were tested in three-electrode electrochemical cells in which lithium strips were used as counter and reference electrodes. A 1 M solution of $LiAsF_6$ in EC:PC (1:1) was used as electrolyte. Cell assembly and electrochemical tests were carried out in a dry room (RH < 1%).

**Equipment and Analysis.** Elemental analyses were carried out at the University of Minnesota Geochemical Lab (metals) and by Atlantic Microlab, Inc., Norcross, GA (C, H, N). The oxidation state of the manganese was determined by reaction with ferrous sulfate solution and subsequent titration with potassium permanganate.[13] Powder X-ray diffraction (XRD) patterns were collected on a Siemens D5005 wide-angle diffractometer with Cu K$\alpha$ radiation. BET surface area measurements were performed by using an Automatic Surface Area Analyzer (Leeds and Northrup Instruments, model 4200). SEM images of the samples dusted onto an adhesive conductive carbon disk were taken on a Hitachi S-800 Electron Microscope. Infrared spectroscopy was performed on a Nicolet Magna-IR 760 FTIR spectrometer with mid-IR and far-IR capability. Spectra were obtained using the powdered sample dispersed in self-supporting KBr wafers for the mid-IR range and polyethylene wafers for the far-IR range. Thermogravimetric analyses (TGA) were performed on a Perkin-Elmer TGA-7 thermal analyzer attached to a PC via a TAC 7/DX thermal controller. Samples were heated under air at 10 °C/min to 800 °C. Galvanostatic experiments were run by using an Arbin Battery Cycler.

## Results and Discussion

**Structural, Morphological, and Elemental Analysis.** Coprecipitation of manganese(II) acetate and sodium nitrate, followed by heat treatment at 400 °C, resulted in a layered sodium manganese oxide phase with a layer spacing of 5.5 Å, as determined by XRD (see Figure 2a). As noted in the Introduction, this phase is described in the literature as a dehydrated form of

(12) Li, L.; Pistoia, G. *Solid State Ionics* **1991**, *47*, 231−240.
(13) (a) Bach, S.; Pereira-Ramos, J. P.; Baffier, N.; Messina, R. *Electrochim. Acta* **1991**, *36*, 1595−1603. (b) Bach, S.; Pereira-Ramos, J. P.; Baffier, N. *J. Electrochem. Soc.* **1996**, *143*, 3429−3434. (c) Bach, S.; Pereira-Ramos, J. P.; Baffier, N. *J. Power Sources* **1997**, *68*, 586−589.
(14) Fritsch, S.; Post, J. E.; Suib, S. L.; Navrotsky, A. *Chem. Mater.* **1998**, *10*, 474−479.
(15) Kanoh, H.; Tang, W.; Makita, Y.; Ooi, K. *Langmuir* **1997**, *13*, 6845−6849.
(16) Luo, J.; Suib, S. L. *J. Phys. Chem. B* **1997**, *101*, 10403−10413.
(17) Kumar, R. *Mater. Trans., JIM* **1994**, *35*, 27−34.
(18) Ching, S.; Roark, J. L.; Duan, N.; Suib, S. L. *Chem. Mater.* **1997**, *9*, 750−754.
(19) Morales, J.; Navas, J. J.; Tirado, J. L. *Solid State Ionics* **1990**, *44*, 125−130.
(20) Shen, X.-M.; Clearfield, A. *J. Solid State Chem.* **1986**, *64*, 270−282.

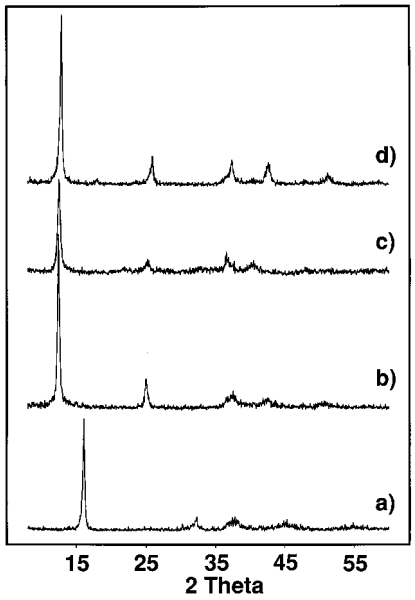


**Figure 2.** Powder XRD patterns of (a) the dehydrated 5.5 Å sodium manganese oxide, (b) Mg−birnessite, (c) Zn−chalcophanite, and (d) Mg−birnessite with 60% of the Mg replaced with lithium.

birnessite, with sodium ions residing between manganese oxide layers.[1,6] All attempts to hydrate this material using water or aqueous solutions of monovalent cations at various temperatures and reaction times produced only mixed systems of the 5.5 Å phase and birnessite. The average oxidation state of the manganese was found to be 3.9 both before and after stirring in water at room temperature for 24 h, implying a high content of Mn(IV) in addition to small amounts of lower valent manganese. Elemental analysis of the water-treated samples showed Na:Mn ratios between 0.45 and 0.53.

Treatment of the 5.5 Å phase with an aqueous solution of $Mg(NO_3)_2$ produced a pure Mg−birnessite phase, as identified by XRD (Figure 2b). The $d_{001}$ and $d_{002}$ peaks are clearly defined for this phase, demonstrating a repeat distance of about 7.1 Å between manganese oxide layers. The remaining peaks are weak and broad, suggesting the samples are only weakly crystalline and possess relatively small domain sizes, similar to observations for natural birnessites. Due to the low crystallinity it was not possible to determine the precise structure of this sample by X-ray diffraction. However, the powder pattern closely matched that of the monoclinic birnessite phase (JCPDS 43-1456), and it appeared to be different from the hexagonal Mg−birnessite phase observed by Bach et al.,[13c] as our sample did not exhibit a $d_{100}$ reflection near 4.86 Å. The powder XRD pattern for the Zn-intercalated sample (Figure 2c) exhibited an additional reflection at $d = 4.06$ Å, characteristic of chalcophanite (JCPDS 45-1320). Powder XRD patterns of samples prepared for electrochemical testing, a preparation which results in partial dehydration of the sample, showed a reduction in peak intensity and indicated that the interlayer water was essential to the stability of the lamellar structure. Efforts to improve crystallinity through heat treatment, concentration variation, and length of ion exchange had little impact. Further, reaction of the 5.5 Å phase with

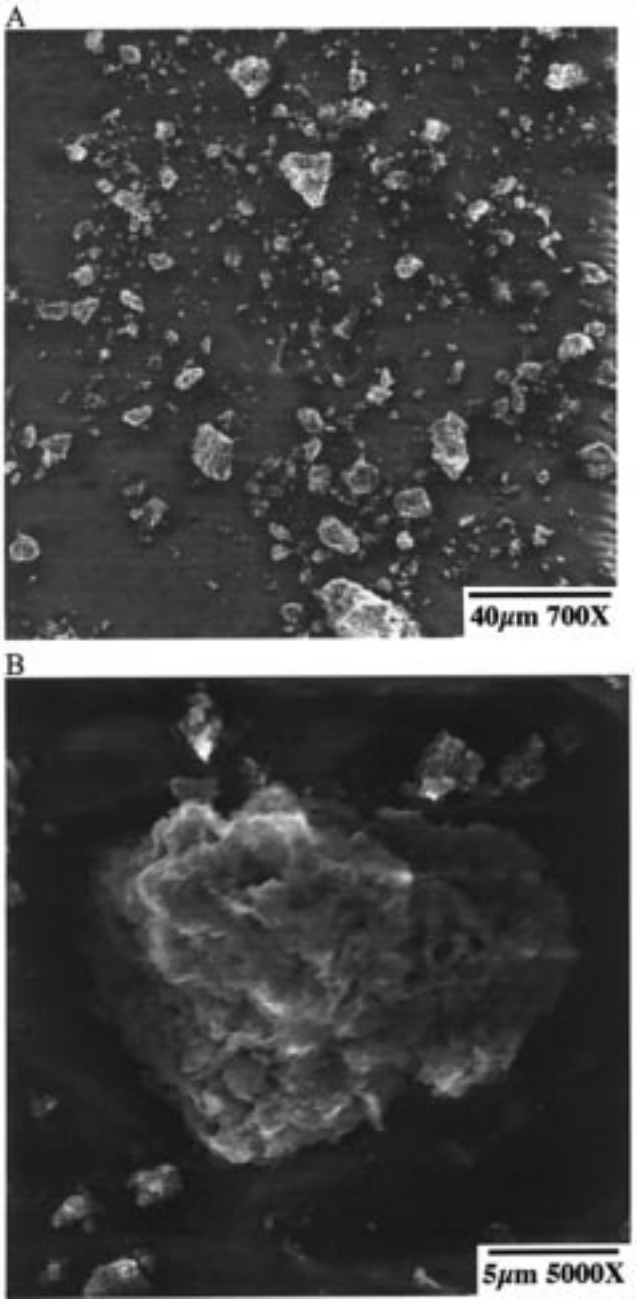


**Figure 3.** SEM images of Mg−birnessite powder under different magnifications.

mono-, di-, and trivalent cations other than $Mg^{2+}$ and $Zn^{2+}$ produced mixtures of lamellar and nonlamellar phases.

Figure 3 shows SEM images of the Mg−birnessite powder. A wide distribution of particle sizes can be observed in the low magnification image (Figure 3A). Most of the particles have diameters ranging from 1 to 5 $\mu$m, but single grains as large as 30 $\mu$m are also seen in the image. The wide spread of particle sizes is the result of the simple procedure (mortar and pestle) used to grind the Na−birnessite after the thermal synthesis. The morphology of a single, medium-size grain is shown in Figure 3B. The particle appears to be an agglomerate of smaller grains. SEM images of the Zn−chalcophanite have shown identical morphology and particle size distribution, indicating that these two characteristics are induced by the thermal synthesis and the subse-

quent soft grinding step and that they are mostly unaffected by the ion exchange process. Single point BET measurements were performed to evaluate the surface area of the two materials. The results were 25 and 14 $m^2/g$ for Zn−chalcophanite and Mg−birnessites, respectively. Such relatively high values of the surface area are typical of manganese oxide materials synthesized at low temperature.[21−24] The qualitative particle size distribution obtained by SEM and the quantitative surface area measurements indicate the existence of an internal porosity in the particles. In particular, the combination of large particle size (>1 $\mu$m), high surface area (>10 $m^2/g$), and high density (>3 $g/cm^3$) supports a morphology characterized by small pores and thin solid phase (a few tens of nanometers).

Elemental analyses indicated that in the Mg−birnessite the exchange between $Na^+$ and $Mg^{2+}$ was incomplete, resulting in the composition $Na^+_{0.26}Mg^{2+}_{0.23}MnO_{2.08}\cdot(CO_3^{2-})_{0.14}\cdot(NO_3^-)_{0.04}\cdot(H_2O)_{0.96}$; the exchange of $Na^+$ with $Zn^{2+}$, on the other hand, was nearly complete, yielding the composition $Na^+_{0.04}Zn^{2+}_{0.50}MnO_{2.33}(CO_3^{2-})_{0.08}(NO_3^-)_{0.05}(H_2O)_{0.96}$ for the Zn−chalcophanite. The average manganese oxidation states for these samples were 3.77 and 3.83, respectively, slightly larger than literature values of 3.64−3.68 for Mg−birnessite[5,13c] and 3.74 for Zn−birnessite.[5] Oxygen-to-manganese ratios greater than 2.0 imply the presence of manganese vacancies in the manganese oxide layers. In the Mg-intercalated sample up to one Mn site out of 26 was vacant in the birnessite structure. In the Zn-intercalated sample the fraction of vacant Mn sites was significantly greater, nearly one in six sites, and the product resembled that of chalcophanite, where one site out of seven is vacant.[7] A residue of carbonate (originating from the acetate-based syntheses) and nitrate ions was present in these samples despite extensive washing. These counterions were confirmed by IR and TGA analyses (see below). Their location could not be firmly established; however, these anions were removed by subsequent ion exchange processes.

The metal cation values obtained appear to represent approximate upper limits to the amount of magnesium and zinc that can be incorporated into the manganese oxides by our synthetic procedure. Alteration of the concentration of the metal ion solution, temperature, or duration of ion exchange did not result in higher Mg and Zn loading. Ion exchange of Mg−birnessite with $LiNO_3$ or $NaNO_3$ permitted replacement of up to 60% magnesium by the new counterion and did not lead to degradation of the layered structure, based on powder XRD data (Figure 2d). Magnesium could also be exchanged with copper(II), nickel, and cobalt(II), although some intensity was lost in the XRD pattern as a result. Ion exchange with ammonium, silver, cadmium, and aluminum cations resulted in complete loss of the layered structure. Interestingly, no zinc could be displaced by ion exchange. Additionally, if the 5.5 Å phase was stirred in an equimolar solution of magnesium and zinc nitrates, the product contained mostly zinc, with only trace amounts of magnesium observed. These results suggest the $Zn^{2+}$ binds more tightly than $Mg^{2+}$ to the $MnO_6$ layers. In previous structural studies of zinc chalcophanite[7] and magnesium birnessite[3] the separation between zinc and oxygen in the Mn−O layer (1.93 and 1.98 Å) was reported to be shorter than the average distance between magnesium and oxygen (2.13 Å).

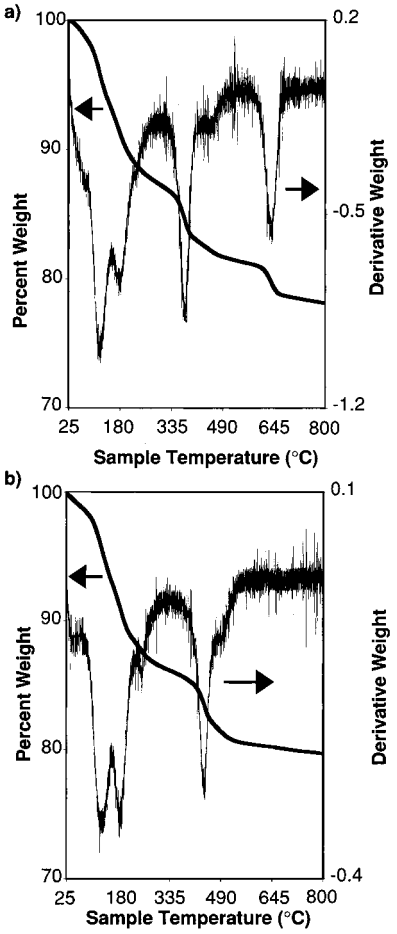


**Figure 4.** TGA of (a) Mg−birnessite and (b) Zn−chalcophanite.

**Thermal Studies.** The thermal analysis curves (Figure 4) were consistent with the chemical formulas obtained by elemental analysis. TGA performed on a sample of Zn−chalcophanite prepared for electrochemical testing (see Experimental Section) showed weight losses at 126, 154, 237, and 433 °C, with an overall weight loss of 19.4%. The overall weight loss for Mg−birnessite was 19.7%, with weight loss occurring at 124, 183, 356, and 635 °C. For both samples, the first weight loss was due to desorption of surface water, and the second loss due to removal of the interlayer water. The total weight loss due to water for Mg− and Zn−manganese oxide was 12.5% and 11.7%, respectively, roughly equal to the values obtained from the elemental analysis. The third weight loss for each sample is attributed to the decomposition of carbonate with loss of carbon dioxide; this is 4.7% weight for the Mg−birnessite and 2.0% for the Zn−chalcophanite. The final weight loss is believed to be due decomposition of nitrate combined with a phase change that results in loss of oxygen from the manganate layers. To confirm the latter

(21) Tackeray, M. M.; David, W. I. F.; Bruce, P. G.; Goodenough, J. B. *Mater. Res. Bull.* **1983**, *18*, 451.
(22) Pistoia, G.; Wang, G. *Solid State Ionics* **1993**, *66*, 135.
(23) Mancini, M. R.; Petrucci, L.; Ronci, F.; Prosini, P. P.; Passerini, S. *J. Power Sources* **1998,** in press.
(24) Xu, J. J.; Kinser, A. J.; Owens, B. B.; Smyrl, W. H. *Electrochem. Solid State Lett.* **1998**, *1*, 1.

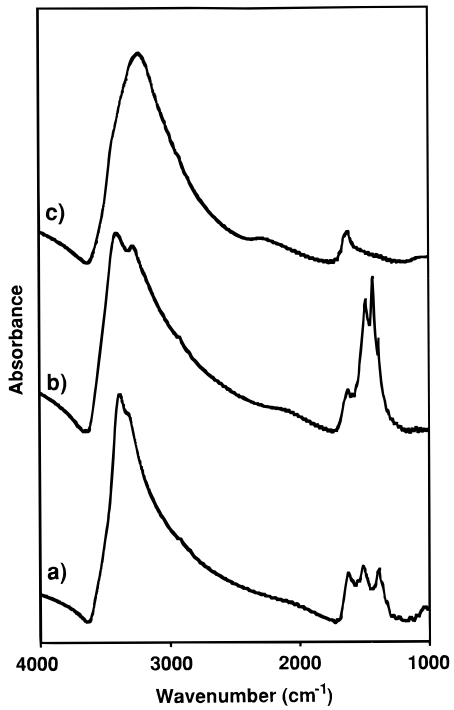


**Figure 5.** IR spectra of (a) Zn−chalcophanite, (b) Mg−birnessite, and (c) Mg−birnessite with 60% of the Mg replaced with lithium.

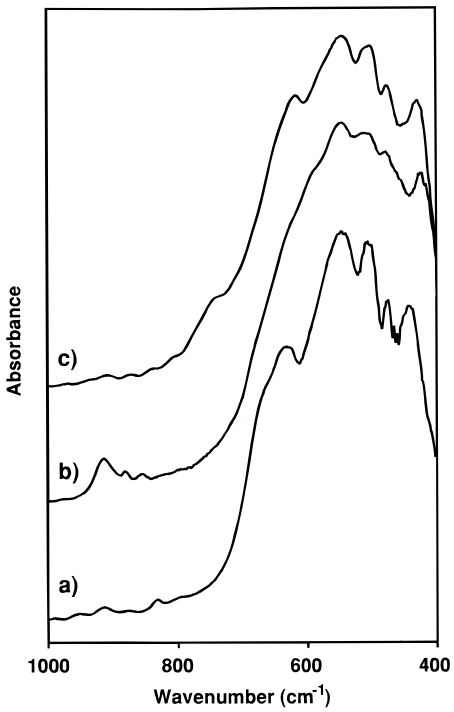


**Figure 6.** IR spectra of (a) Zn−chalcophanite, (b) Mg−birnessite, and (c) Mg−birnessite with 60% of the Mg replaced with lithium.

hypothesis, samples of Mg−birnessite and Zn−chalcophanite were heated at 10 °C/min to 800 °C under air, resulting in the formation of $ZnMn_2O_4$ and $MgMn_2O_4$ spinel phases.

It was noted earlier that $Zn^{2+}$ ions bind more tightly to the manganese framework than $Mg^{2+}$ ions. As bonding interactions are shared among the framework, metal ions, and interstitial water, stronger $Zn^{2+}$−manganese framework binding is expected to weaken the interactions between $Zn^{2+}$ and water, thus leading to the lower water desorption temperatures observed in the TGA, compared to Mg−birnessite. Water desorption takes place at higher temperatures for the samples analyzed in this report, relative to those reported in the literature on Na− and K−birnessite,[2,5,6] although it compares fairly well for Mg−birnessite.[16]

**Infrared Analysis.** IR spectra confirmed the assignment of the metal-exchanged manganese oxide phases to Zn−chalcophanite and Mg−birnessite. Chalcophanite exhibits IR absorptions in the O−H stretching region and in the 550−400 $cm^{-1}$ region that distinguish this phase from other manganese oxides.[8] The IR spectrum of the Zn−chalcophanite obtained by the low-temperature synthesis (Figure 5a) shows peaks at 3388 and 3309 $cm^{-1}$, which are attributed to symmetric and asymmetric stretching vibrations of interlayer water molecules.[4] The water peaks are separated farther for the Mg−birnessite (Figure 5b), appearing at 3408 and 3285 $cm^{-1}$, while the partially Li-exchanged sample exhibited only one water peak at 3235 $cm^{-1}$ (Figure 5c). Although the peaks due to O−H stretching are broad, the fact that they can be resolved indicates that the water−cation interaction and the physical restriction of the layers imposes some degree of order upon the water molecules. Upon partial lithium exchange, the two peaks merge into one absorption, consistent with a reduction in the order of the interlayer water molecules by the presence of the additional cation. The peak at 1630 $cm^{-1}$ is ascribed to O−H bending vibrations of the intercalated water molecules.[20] An absorption peak at 1429 $cm^{-1}$ in the Mg−birnessite and peaks at 1385−1388 $cm^{-1}$ in both Mg- and Zn-intercalated samples are assigned to carbonate C−O stretching and nitrate N−O stretching vibrations. These bands disappear after partial lithium exchange.

IR absorptions at 547, 505, and 477 $cm^{-1}$ are observed for Zn−chalcophanite, Mg−birnessite, and Li-exchanged Mg−birnessite (Figure 6) and are assigned to Mn−O vibrations.[4,8] All known layered manganese oxides have a strong band in the 400−450 $cm^{-1}$ region.[8] The position of this band distinguished the three samples; it occurred at 443 $cm^{-1}$ for the Zn−chalcophanite sample, 423 $cm^{-1}$ for the Mg−birnessite sample, and 430 $cm^{-1}$ for the Li-exchanged sample. An additional peak at 634 $cm^{-1}$ in Zn−chalcophanite and 618 $cm^{-1}$ in Li-exchanged Mg−birnessite suggested further variations in local structure between the three samples, probably related to the differences in the fraction of Mn vacancies.

**Electrochemical Characterization.** The electrochemical properties of the Mg−birnessite and Zn−calcophanite samples as lithium hosts were characterized by means of galvanostatic experiments in which constant currents were passed through electrochemical cells containing the materials under investigation. Charge and discharge rates are commonly used to define the experimental conditions. They are dimensionally equivalent to current and are expressed as $C/n$, where $C$ is the nominal capacity of the cell and $n$ is the time, in hours, in which the nominal capacity would be utilized at that rate. In addition, they are independent of the active material loading as well as the electrode area. The values quoted in this report are calculated assuming the insertion of 1 equiv of lithium per equivalent of Mn as the nominal capacity.

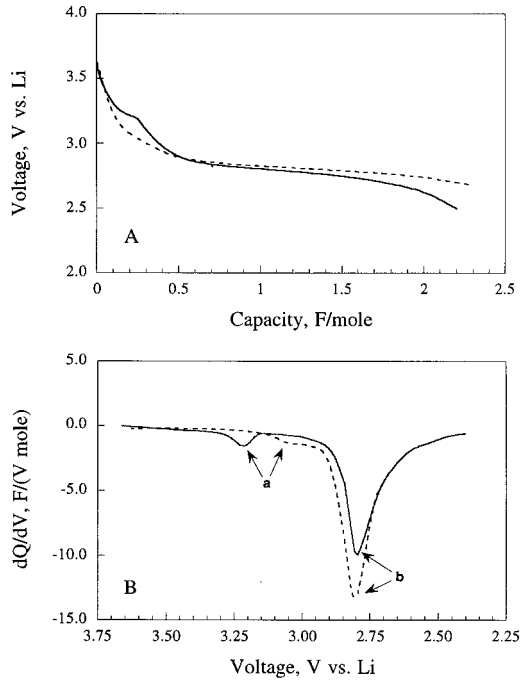


**Figure 7.** Low rate (C/200) galvanostatic discharge of Zn−chalcophanite (solid line) and Mg−birnessite (dashed line) composite cathodes. Panel A illustrates the voltage vs capacity behavior. Panel B shows the computed differential capacity vs voltage. End-of-discharge voltage: 2.5 V (vs Li). Conditions: counter and reference electrodes: lithium; electrolyte, 1 M $LiAsF_6$ in EC:PC (1:1); ambient temperature.

The maximum lithium insertion capacity of the samples was examined by slowly driving the intercalation process. The upper plot in Figure 7 shows the voltage behavior during the first discharge of Mg−birnessite and Zn−chalcophanite composite pellets. The cells were discharged at C/200 rate that corresponded to a current of about 0.007 mA or a current density of 0.021 mA/cm$^2$. Mg−birnessite and Zn−chalcophanite were able to host up to 2.3 and 2.2 equiv of lithium per manganese that correspond to a delivered capacity of 560 and 440 (mA h)/g, respectively. The related specific energy was 1600 and 1250 (mW h)/g, respectively. The excellent insertion performance compares very well with spinel $LiMn_2O_4$,[21−23] amorphous manganese oxyiodide[25] and layered $LiMnO_2$,[26] as well as other birnessites.[5,10,11,13] The largest insertion capacity reported for birnessites, in similar discharge conditions,[5,10,11,13] was lower than 1 equiv of lithium per mole of active material.

The discharge curves of the Zn−chalcophanite and Mg−birnessite composite cathodes (Figure 7, upper plot) show poorly defined regions, each of them characterized by a low voltage slope (plateau). The presence of different plateaus during the first discharge of the layered manganese oxides is indicative of different processes associated with the initial lithium insertion. To investigate this possibility, differential capacity vs voltage curves of the Mg−birnessite and Zn−chalcophanite composite cathodes were computed from the C/200 discharge results and are reported in the lower plot of Figure 7. Both materials showed two distinct peaks (labeled as a and b in the figure) correlated with two different processes.

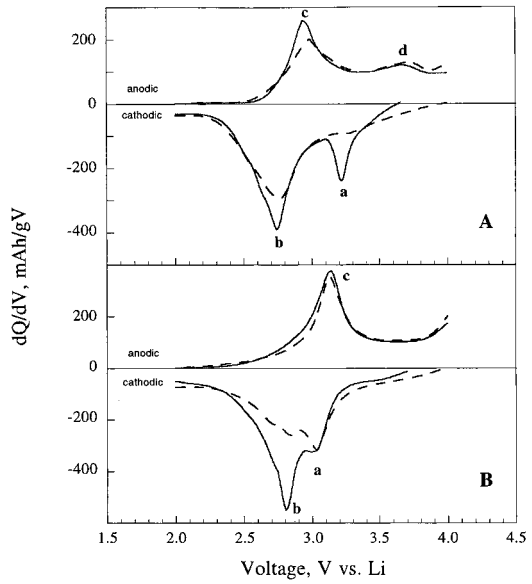


**Figure 8.** Differential capacity vs voltage plot of Zn−chalcophanite (panel A) and Mg−birnessite (panel B) composite cathodes during the first (solid lines) and second (dashed lines) galvanostatic cycles. For an easier comprehension of the figure, the differential capacities computed over the cathodic semi-cycles are reported with a negative sign. Conditions: rate, C/40; voltage limits, 2.0 and 4.0 V (vs Li); counter and reference electrodes, lithium; electrolyte, 1 M $LiAsF_6$ in EC:PC (1:1); ambient temperature.

To investigate the lithium insertion process further, continuous galvanostatic cycle tests were performed at a higher rate (C/40). The differential capacity vs voltage curves computed for the initial and the second cycles are illustrated in Figure 8. Useful information on the materials is obtained by comparing the curves in Figure 7B and in Figure 8. The relative intensities of the peaks in the differential capacity curves of, for example, Zn−chalcophanite strongly depend on the discharge rate used. This behavior also indicates that the insertion step which proceeds at lower voltage is characterized by slower kinetics.

Further analysis of the cycling evolution of the differential capacity curves in Figure 8 gives information on the reversibility of the two processes. For example, Zn−chalcophanite (panel A) showed the first cathodic peak (a) at 3.22 V (vs Li) and the second one (b) at 2.74 V (vs Li). Upon lithium release (solid line, anodic side), two anodic peaks (c and d) were also seen at 2.95 and 3.70 V (vs Li), respectively. It is worth noting the broadness and weakness of the anodic peak d. During the second cycle, peak a sharply decreased in intensity and it completely disappeared on the following cycles (not shown). On the other hand, peaks b and c remained almost constant both in position and intensity. On the basis of these results, it is possible to correlate the peaks b and c to a reversible lithium insertion/release process and peak a to a mostly irreversible process. The b to c peak separation, i.e., the voltage difference between the center of the cathodic and the anodic peaks, is only slightly above 200 mV. This is a further indication of a good reversibility of the insertion and release of lithium in the Zn−chalcophanite sample.

The differential capacity plot of the Mg−birnessite composite cathode is substantially similar (Figure 8, panel B) to that of Zn−chalcophanite. The only differ-

(25) Kim, J.; Manthiram, A. *Nature* **1997**, *390*, 265.
(26) Armstrong, A. R.; Bruce, P. G. *Nature* **1997**, *390*, 265.

ence consists of the positions of the peaks a and d (peaks are labeled consistently with panel A). The irreversible peak a is located at a lower voltage, 3.03 V (vs Li) while peak d is either absent or located close to the upper voltage limit.

The nature of the irreversible cathodic process that takes place in the substituted manganese oxides is not completely clear yet. Most studies on birnessites showed substantial capacity fadings upon the initial cycles.[5,10,11,13] The enhanced lithium insertion capacity of Bi-substituted birnessites has been associated with the pillaring effect of large cations and the contemporaneous presence of water molecules that stabilize the layered structure.[11] In Mg−birnessite, the irreversible peak (3.03 V (vs Li)) is shifted to voltages lower than those for Zn−chalcophanite (3.22 V (vs Li)). The comparison of the peak a position in the two substituted manganese oxides shows a substantial shift of the peak toward lower voltages (>200 mV) in the magnesium-substituted material. A number of factors may contribute to the observed difference of the irreversible peak position (a in Figure 8). The difference could be related to specific host−guest interactions due to the displacement of the substituting cations (Mg or Zn), due to the different number of Mn vacancies in the Mg−birnessite and Zn−chalcophanite structures, or it could be associated with an interaction with the interlayer water present in the materials. In fact, the irreversible peaks are positioned in a voltage range (3.22 and 3.03 V (vs Li) for Zn− and Mg−birnessites, respectively) suitable for the water reduction reaction. The difference in peak potential shown by the two birnessites is consistent with the results of the TGA experiments that indicate a stronger bonding of the interlayer water molecules in Mg−birnessite. This evidence supports the proposed correlation between the interlayer water and the irreversible capacity, but further experiments are needed to fully clarify the nature of the irreversible process.

To acquire a more comprehensive picture of the performance of Mg−birnessite and Zn−chalcophanite as lithium insertion cathodes, kinetic tests (rate performance) were also performed. The results are shown in Figure 9, which illustrates the voltage behavior of the composite electrodes upon constant current discharges at different rates. The cells were always recharged at a C/40 rate in order to fix the initial state of charge of the electrodes. The related delivered capacity and the specific energy of the materials are reported in Table 1. Both materials showed a sharp decline of performance with respect to the very low rate discharge tests illustrated earlier. The highest specific energy, obtained at the lowest rate C/40, was about 660 (mW h)/g for Mg−birnessite and 550 (mW h)/g for Zn−chalcophanite. The capacity decrease is due to kinetic limitations associated with the morphology of the materials. As shown earlier, the intercalated manganese oxides are characterized by a porous morphology where both the pore diameter and the dimensions of the solid phase are relatively small. These characteristics are detrimental to the rate performance. Small pores are flooded by the electrolyte with difficulty. Furthermore, the concentration of the $Li^+$ ions in the electrolyte within the pores is quickly depleted if the insertion of the ions in the host material solid phase is driven above the

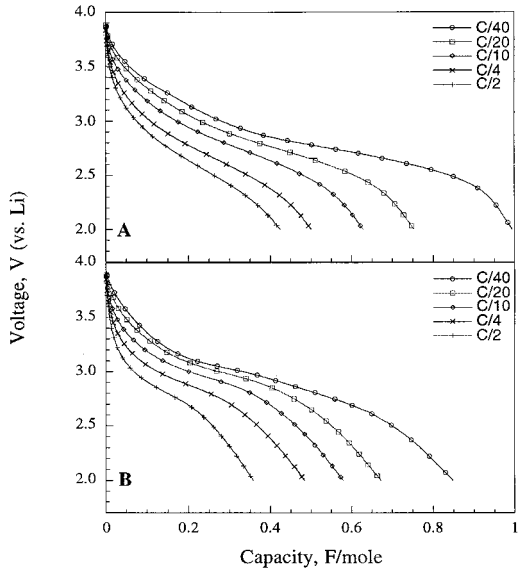


**Figure 9.** Effect of the discharge rate on the insertion capacity of Zn−chalcophanite (panel A) and Mg−birnessite (panel B) composite cathodes upon galvanostatic lithium intercalation. The curves show the voltage vs capacity behavior upon discharges driven at different rates from C/40 to C/2. The cells were always recharged at the lowest rate (C/40 rate). Conditions: voltage limits, 2.0 and 4.0 V (vs Li); counter and reference electrodes, lithium; electrolyte, 1 M $LiAsF_6$ in EC:PC (1:1); ambient temperature.

**Table 1. Delivered Capacity and Specific Energy of Zn−Chalcophanite and Mg−Birnessite Composite Cathodes upon Galvanostatic Discharges at Various Rates[a]**

| | Zn−chalcophanite | | Mg−birnessite | |
|---|---|---|---|---|
| rate | specific capacity, (mA h)/g | specific energy, (mW h)/g | specific capacity, (mA h)/g | specific energy, (mW h)/g |
| 2 | 85 | 225 | 95 | 260 |
| 4 | 100 | 270 | 130 | 360 |
| 10 | 120 | 340 | 155 | 440 |
| 20 | 145 | 415 | 180 | 520 |
| 40 | 190 | 550 | 230 | 660 |

[a] The cells were always recharged at the lowest rate (C/40 rate). Conditions: voltage limits, 2.0 and 4.0 V; counter and reference electrodes, lithium; electrolyte, 1 M $LiAsF_6$ in EC:PC (1:1); ambient temperature.

(pore) limiting current. For the intercalation process to proceed at high rate conditions, the lithium must diffuse in the solid phase of the material away from the current collector. The diffusion process is then parallel to the pores, i.e., the lithium ions and the associated electrons must diffuse into the long, thin solid phase. The diffusion thickness is roughly equivalent to the particle size (>1 $\mu$m) and the cross section of the diffusion path coincides with the thin solid phase (a few tens of nanometers). Nevertheless and despite the described limitations, Mg−birnessite composite cathodes were able to deliver a capacity as high as 130 (mA h)/g with a corresponding specific energy of more than 360 (mW h)/g even at very high rate (C/4). This rate corresponded to an actual current in the cell of ~0.3 mA or a current density of ~0.9 mA/cm$^2$.

The effect of the upper cutoff (anodic limit) on the insertion capacity of the Mg−birnessite and Zn−chalcophanite composite cathodes upon high rate (C/4) galvanostatic cycles was also studied. The results are

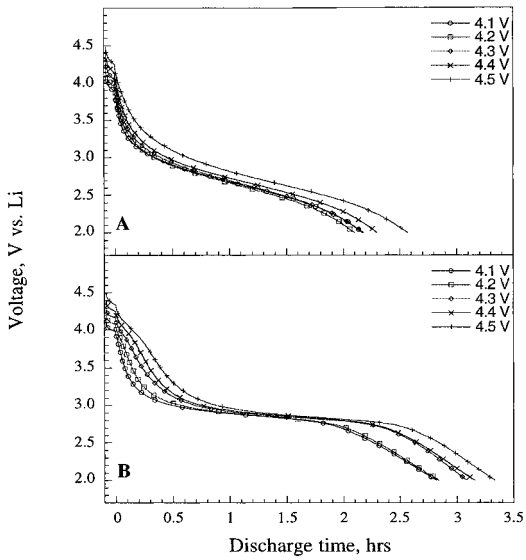


**Figure 10.** Effect of the upper cutoff on the delivered capacity of Zn−chalcophanite (panel A) and Mg−birnessite (panel B) composite cathodes upon galvanostatic lithium insertion/deinsertion cycles. The curves show the voltage vs time behavior for different values of the anodic voltage cutoff. The cells were charged and discharged at C/4 rate with a cathodic voltage cutoff fixed at 2 V (vs Li). Conditions: counter and reference electrodes, lithium; electrolyte, 1 M $LiAsF_6$ in EC:PC (1:1); ambient temperature.

shown in Figure 10, which illustrates the discharge behavior for different anodic cutoff limits. Both materials showed increases of the discharge capacity. The capacity of the Zn−chalcophanite composite cathode increased from 0.47 F/mol when cycled in the voltage range from 2.0 to 4.0 V (vs Li), to 0.60 F/mol in the 2.0−4.5 V (vs Li) range. Within similar cycle voltage ranges, the specific capacity of Mg−birnessite rose from 0.61 to 0.71 F/mol. The increased discharge capacity upon increasing voltage cutoffs is due to the larger extraction of intercalated lithium during the recharge. The materials were then able to support larger lithium insertion levels (delivered capacity) in the following discharges.

The cycle performance of the materials was also evaluated by continuous galvanostatic charge/discharge cycling in the 2.0−4.0 V (vs Li) range. The results are illustrated in Figure 11 where the charge and discharge capacities of the composite cathodes are reported upon repetitive cycles at C/10 rate. For the sake of clarity, the results of only one cell for each material are shown in the figure, but they were reproduced for several cells. The cycle performance did not differ for composite cathodes with Mg−birnessite or Zn−chalcophanite, although the initial delivered capacity differed substantially (∼200 (mA h)/g for Mg−birnessite and ∼150 (mA h)/g for Zn−chalcophanite). Both materials showed fairly good cycle performance. The average capacity fading was about 2.5% (per cycle) over the first 10 cycles, and it decreased to less than 0.2% (per cycle) after the 20th cycle. After 40 cycles, the Mg−birnessite composite cathode was able to deliver about 140 (mA h)/g and after 80 cycles the delivered capacity was still above 125 (mA h)/g. In comparison, a previously synthesized hexagonal Mg−birnessite with a lower Mg content (0.14 Mg/Mn) and a lower average Mn oxidation state (3.64) exhibited an initial capacity of 130 (mA h)/g which decreased to ∼120 (mA h)/g after 20 cycles at C/20 discharge.[13c] Our

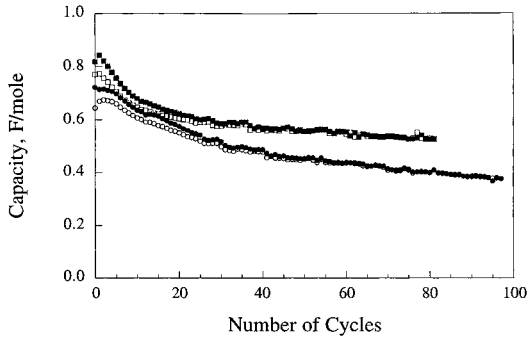


**Figure 11.** Cycle performance of Zn−chalcophanite (circles) and Mg−birnessite (squares) composite cathodes upon galvanostatic lithium insertion/deinsertion cycles. Solid markers and open markers indicate discharge and charge capacities, respectively. The cells were always charged and discharged at C/10 rate. Conditions: voltage limits, 2.0 and 4.0 V (vs Li) (exceptions to these limits are specified in the text); counter and reference electrodes, lithium; electrolyte, 1 M $LiAsF_6$ in EC:PC (1:1); ambient temperature.

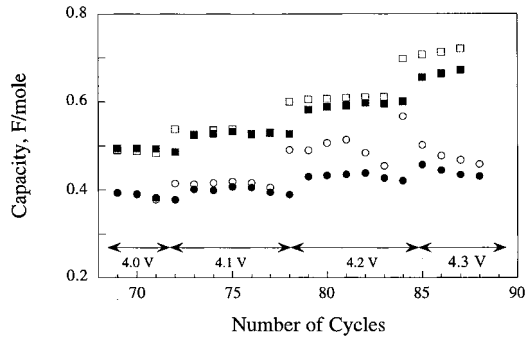


**Figure 12.** Effect of anodic cutoff on the cycle performance of Zn−chalcophanite (circles) and Mg−birnessite (squares) composite cathodes upon galvanostatic lithium insertion/deinsertion cycles. Solid markers and open markers indicate discharge and charge capacities, respectively. Conditions: charge/discharge rate, C/10; cathodic voltage limit, 2.0 V (vs Li); anodic voltage cutoff, specified in the figure; counter and reference electrodes, lithium; electrolyte, 1 M $LiAsF_6$ in EC:PC (1:1); ambient temperature.

results are very promising, considering that the cycle performance is expected to improve by morphological (particle size of the starting materials), compositional and engineering optimizations.

The effect of one of the possible optimization methods, the selection of the voltage cutoff upon charge, is shown in Figure 12. The plot illustrates the delivered capacity of the two birnessites as a function of the anodic cutoff voltage. The anodic cutoff of the cells was progressively increased by 0.1-V steps up to 4.3 V (vs Li) (to avoid any influence on the measurements originated by the capacity fading, the cells were previously stabilized by continuous cycling at C/10 rate over the 2.0−4.0 V voltage range). As a result of the wider voltage range, both materials showed an increase of delivered capacity (see Figure 12 and Table 2) but the enhancement was larger in Mg−birnessite than in Zn−chalcophanite composite cathodes. The former material was able to deliver above 160 (mA h)/g when charged up to 4.3 V (vs Li). The lower capacity increase of the Zn−chalcophanite composite cathode upon increasing anodic cutoffs can be understood from the behavior of the charge capacity and the cycle efficiency (the ratio of discharge/charge capacity) reported in Figure 12 and

**Table 2. Discharge Capacity and Cycle Efficiency of Zn−Chalcophanite and Mg−Birnessite Composite Cathodes upon Galvanostatic Cycles with Different Values of the Anodic Voltage Cutoff (Right Axis)[a]**

| | Zn−chalcophanite | | | | Mg−birnessite | | | |
|---|---|---|---|---|---|---|---|---|
| anodic cutoff, V | discharge at 2nd cycle, F/mol | cycle efficiency | discharge at 6th cycle, F/mol | cycle efficiency | discharge at 2nd cycle, F/mol | cycle efficiency | discharge at 6th cycle, F/mol | cycle efficiency |
| 4.0 | | | 0.382 | 1.000 | | | 0.493 | 1.000 |
| 4.1 | 0.401 | 0.972 | 0.395 | 0.975 | 0.524 | 0.996 | 0.529 | 0.998 |
| 4.2 | 0.430 | 0.879 | 0.427 | 0.939 | 0.582 | 0.961 | 0.596 | 0.976 |
| 4.3 | 0.457 | 0.911 | 0.430 | 0.931 | 0.656 | 0.928 | 0.665 | 0.933 |

[a] The cells were charged and discharged at C/10 rate with a cathodic voltage cutoff fixed at 2 V (vs Li). Conditions: counter and reference electrodes, lithium; electrolyte, 1 M $LiAsF_6$ in EC:PC (1:1); ambient temperature.

Table 2, respectively. For voltage cutoffs larger than 4.1 V (vs Li), the behavior of the Zn−chalcophanite charge and discharge capacities was somewhat erratic. Upon an increase of the voltage cutoff, both quantities initially increased (see Table 2, second cycle) but then lowered substantially. In addition, the cycle efficiency sharply lowered for increasing voltage cutoffs. Both results indicate that a substantial fraction of the current passing through the cell during the charge at voltages above 4.1 V (vs Li) was consumed in an irreversible process, most likely electrolyte decomposition. Only part of the current contributed to the lithium-releasing process (deintercalation). On the other hand, the cycle efficiency of the Mg−birnessite composite cathode remained very high (∼98%) even with the 4.2 V (vs Li) cutoff. This allowed for a larger release of intercalated lithium during the recharge and then a larger insertion (delivered capacity) in the following discharge.

## Conclusions

A new procedure to synthesize magnesium-substituted birnessite and zinc chalcophanite has been developed. It is based on a combination of two simple techniques, coprecipitation and metal ion intercalation. The materials prepared through the new procedure were seen to maintain the layered structure typical of birnessites.

The electrochemical characterization of Mg−birnessite and Zn−chalcophanite as host materials for lithium intercalation has shown very promising performance. The maximum insertion capacity of the materials, evaluated from the first discharge at low current density, was 2.3 and 2.2 F/mol, respectively. Although a fraction of the first cycle capacity appeared to be associated with an irreversible process, a fairly high capacity of about 1 equiv of lithium per mole of birnessite was obtained at the second cycle.

Despite kinetic limitations due to the nonoptimized morphology, Mg−birnessite composite cathodes showed fairly good rate performance by delivering capacity as high as 130 (mA h)/g and specific energy of more than 350 (mW h)/g in C/4 rate discharge. The combination of thermodynamic and kinetic properties exhibited by the substituted birnessites compare well with other manganese oxides and these properties are expected to improve upon morphological, compositional, and engineering optimizations.

Of further importance, the synthesis procedure as well as the materials involved are both environmentally safe and inexpensive as compared with those currently in use. These factors, combined with the high capacity and energy performance, contribute to lower the cost of the final devices, the rechargeable lithium batteries.

**Acknowledgment.** 3M, Dupont, the David and Lucille Packard Foundation, the McKnight Foundation, the National Science Foundation (DMR-9701507), and DOE (DE-FG02-93ER14384) are acknowledged for support of this research.

CM9805828